eprints@whiterose.ac.uk
https://eprints.whiterose.ac.uk/

# Boundary effects and the onset of Taylor vortices

## A.M. Rucklidge

*Department of Applied Mathematics, University of Leeds, Leeds LS2 9JT, UK*

and

## A.R. Champneys

*Department of Engineering Mathematics, University of Bristol, Bristol BS8 1TR, UK*

## Abstract

It is well established that the onset of spatially periodic vortex states in the Taylor–Couette flow between rotating cylinders occurs at the value of Reynolds number predicted by local bifurcation theory. However, the symmetry breaking induced by the top and bottom plates means that the true situation should be a disconnected pitchfork. Indeed, experiments have shown that the fold on the disconnected branch can occur at more than double the Reynolds number of onset. This leads to an apparent contradiction: why should Taylor vortices set in so sharply at the Reynolds number predicted by the symmetric theory, given such large symmetry-breaking effects caused by the boundary conditions? This paper offers a generic explanation. The details are worked out using a Swift–Hohenberg pattern formation model that shares the same qualitative features as the Taylor–Couette flow. Onset occurs via a wall mode whose exponential tail penetrates further into the bulk of the domain as the driving parameter increases. In a large domain of length $L$, we show that the wall mode creates significant amplitude in the centre at parameter values that are $O(L^{-2})$ away from the value of onset in the problem with ideal boundary conditions. We explain this as being due to a Hamiltonian Hopf bifurcation in space, which occurs at the same parameter value as the pitchfork bifurcation of the temporal dynamics. The disconnected anomalous branch remains $O(1)$ away from the onset parameter since it does not arise as a bifurcation from the wall mode.
© 2003 Elsevier B.V. All rights reserved.

*Key words:* Pattern formation; Boundary effects; Taylor–Couette flow; Anomalous modes. 47.20.Ky; 47.54.+r.

# 1 Introduction

The Taylor–Couette experiment provided one of the first quantitative verifications of the correctness of the Navier–Stokes partial differential equations (PDEs) describing the dynamics of fluid flows. The experiment, in its simplest form, consists of a pair of concentric cylinders with a fluid-filled gap in between; as the inner cylinder is rotated, a shearing flow (the Couette flow) is established between the cylinders, and this becomes unstable to axisymmetric rolls (Taylor vortices) at a critical value of the rotation rate (as measured by a dimensionless Reynolds number $R$). See [1–4] for reviews. One notable achievement of Taylor's work [5] in 1923 was the theoretical prediction and the experimental measurement of the critical Reynolds number $R_c$ for the onset of vortices, with remarkably good agreement between the two. In doing the stability calculation, Taylor assumed that the vortices would be periodic in the direction along the axis, and neglected the effects of the top and bottom plates of the experiment. With this assumption, the bifurcation leading to Taylor vortices is a pitchfork (figure 1(a)), and the characteristic sharp transition of this bifurcation, with the strength of the vortices going as the square root of the degree of supercriticality $R - R_c$, has been confirmed experimentally [6]. The symmetry that is broken in this pitchfork is a translation symmetry along the axes of the cylinders.

Subsequent theoretical developments explored the role of the top and bottom plates in the experiment, which spoil the idealisation of spatial periodicity in the direction parallel to the axis of rotation, and which break the translation symmetry assumed in the original theoretical work. Ekman boundary layers cause the fluid near the boundary to spiral preferentially inwards for any non-zero rotation rate, and the Taylor vortices to develop first in the boundary layer, moving smoothly into the bulk of the fluid as $R$ approaches $R_c$ – this has been observed in experiments [9] and in calculations [10]. In the words of Benjamin [7], 'no precise critical value of $R$ exists for the onset of cellular motion'. Benjamin [7] interpreted the formation of Taylor vortices as a broken pitchfork (figure 1(b)), with the end plates driving a flow near the boundary for all non-zero $R$, and this flow exciting a cellular flow that penetrates the central region with increasing Reynolds number – see figure 2.

The qualitative role of the end boundaries was explored further by Schaeffer [12], who introduced a homotopy parameter $\tau$ ($0 \leq \tau \leq 1$). Here $\tau = 0$ corresponds to ideal end boundary conditions, where a state of pure Couette flow exists for all values of $R$, $\tau = 1$ corresponds to physically realistic end boundary conditions, and intermediate values of $\tau$ interpolate between these
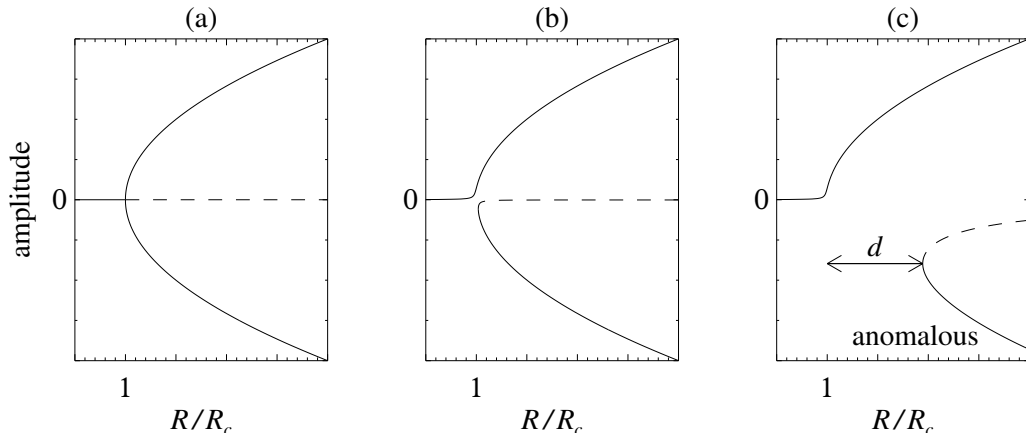
2

Fig. 1. Sketches of the amplitude of Taylor vortices measured in the centre of the apparatus as a function of Reynolds number $R$, under various assumptions. (a) With ideal (reflecting or periodic) boundary conditions, there is a sharp transition to Taylor vortices at a pitchfork bifurcation at $R = R_c$. (b) With the assumption of a weakly broken pitchfork bifurcation, there is still a relatively sharp onset of Taylor vortices close to $R = R_c$ (after [7]); (c) The experiments of Benjamin and Mullin [8] suggest that the upper half is still a weakly broken pitchfork, whereas the lower half is a strongly broken pitchfork, with anomalous modes only appearing at Reynolds numbers at least twice the critical value. Solid (dashed) lines indicate stable (unstable) solutions.
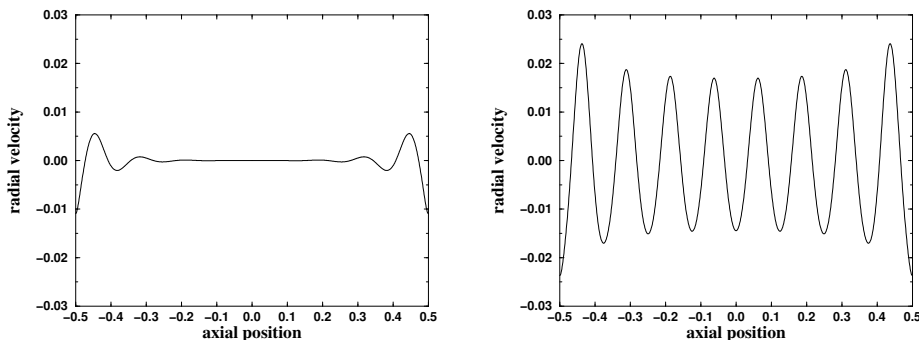


Fig. 2. Finite-element results, reproduced with permission from [11], showing two steady radial velocity profiles below and above the critical value of $R$ at which the onset of periodic vortices would occur with periodic boundary conditions. (a) $R/R_c = 63.74/68.189 = 0.935$; (b) $R/R_c = 69.02/68.189 = 1.013$.

two extremes. The results for $\tau$ close to zero are indeed consistent with a weakly broken pitchfork bifurcation (figure 1(b)), and are in qualitative agreement with experimental results of Benjamin [7,13]. That is, as the Reynolds number is increased slowly, vortices grow smoothly, with the most rapid growth occurring for $R$ close to the critical value. This is illustrated in figure 2. Note how the radial velocity profiles are not zero for $R$ below $R_c$. Instead we see a pair of 'wall modes' connecting the non-parallel flow at the walls to Couette

flow in the main body of the cylinder. Similarly, the steady solution for $R$ greater than $R_c$ is not a pure periodic solution but has modulation near the two walls in order to satisfy the inhomogeneous boundary conditions.

However, by starting the experiment impulsively, it is possible to find another branch of vortices (*anomalous modes*) that resemble ordinary vortices, but have the opposite sign – close to the ends, these anomalous vortices have an outwards radial velocity, opposite to the normal vortices [13]. Other experiments and calculations indicate that anomalous modes may also have stagnation regions or narrow counter-cells close to the top and bottom boundaries [14,15].

However, anomalous modes cannot be found close to the critical Reynolds number, as would be suggested by figure 1(b). Instead, $R$ needs to be significantly increased from its critical value (and the cylinder started impulsively) before anomalous modes can be found [8]. Once they are established, the anomalous modes persist as $R$ is decreased to a lower stability bound, the exact value of which depend on experimental parameters such as the gap width between the inner and outer cylinders, or the aspect ratio $L$, a dimensionless measure of the length of the column. The lower existence boundary appears always to be at least twice the critical value $R_c$ [8], and can be much higher if the gap between the cylinders is narrow [16]. Thus the experimental situation is depicted in figure 1(c). Interestingly, the lower stability boundary of the anomalous modes seems to be independent of aspect ratio (for sufficiently large $L$), and remains at an appreciable multiple of the critical Reynolds number for ordinary modes even as $L \to \infty$ [16,17]. This emphasises the fact that the large (but finite) aspect ratio limit is very different from the idealisation of periodicity in the axial direction.

It is worth emphasising the two surprising and apparently contradictory aspects that have emerged. First, the distance ($d$ in figure 1(c)) between the fold on the disconnected (anomalous) branch and the onset of ordinary Taylor vortices is such that the Reynolds number at the fold is at least a factor of two larger than the Reynolds number at onset. Making the cylinder longer (so that the boundary effects are moved 'towards infinity') does not make $d$ tend to zero, and many authors have concluded that the onset of Taylor vortices can in no way be regarded as a weakly broken pitchfork. Second, the onset of vortices is sharp when viewed in terms of measures such as the radial velocity of the midpoint of the apparatus, and it occurs at almost exactly the value of $R$ that is predicted for the problem without end effects – so the onset of Taylor vortices apparently can be described as a weakly broken pitchfork bifurcation. This discrepancy would not be expected for a generic unfolding of a pitchfork bifurcation. The purpose of the present paper is to explain this apparent contradiction.

4

The rest of the paper is outlined as follows. In section 2, we introduce the Swift–Hohenberg equations as a model for the Taylor–Couette flow. We note that the modification of pattern formation due to the presence of weak forcing at lateral boundaries in Swift–Hohenberg equations has been addressed in the work of Daniels and co-workers [18,19] with application to Rayleigh–Bénard convection in mind. In contrast with their work, we include an $O(1)$ boundary condition that forces the flow strongly. This approach is also distinguished from approaches based on using the Ginzburg–Landau equation for the envelope of the vortex amplitude [20,21]. Indeed, Ahlers *et al.* [21] obtained quantitative agreement with experimental measurements of the onset of Taylor vortices, using the Ginzburg–Landau equation with an $O(1)$ inhomogeneous boundary condition, inspired by earlier work of [22]. However, the Ginzburg–Landau approach does not capture the anomalous modes, and so cannot be used to resolve the contradiction described above.

Section 3 then presents an analysis of the linearised version of this model. Despite being purely linear, it is found that mode shapes like those in figure 2 emerge under static increase of the bifurcation parameter through the value at which the symmetric problem bifurcates. We explain this in terms of the relation between the temporal pitchfork bifurcation and a spatial Hamiltonian Hopf bifurcation.

Section 4 goes on to consider a nonlinear bifurcation analysis. It transpires that the unfolded pitchfork resembles figure 1(c). There are many disconnected branches that emerge from primary and secondary symmetry breaking bifurcations in the symmetric problem. In the Swift–Hohenberg example studied in detail, one of these branches can be identified as the stable anomalous mode, but we find that it does not always emerge from the primary pitchfork bifurcation when the symmetry-breaking terms tend to zero. We explore this issue in some detail. Finally, section 5 draws conclusions and discusses wider implications of the results.

## 2   Swift–Hohenberg model

Rather than consider the nonlinear axisymmetric hydrodynamic partial differential equations (PDEs) that describe the flow between two rotating cylinders, we focus on the simpler Swift–Hohenberg [23] PDE, which shares many of the same pattern-forming features. In fact, Melbourne [24] has demonstrated that bifurcation problems of the Taylor–Couette type (steady state bifurcations with nonzero critical wavenumber in systems with Euclidean symmetry) reduce to equations of Swift–Hohenberg form (though with more general non-

linear terms). The model equation we use is:

$$U_t = \mu U - (U + 2U_{xx} + U_{xxxx}) - U^3 - U\,U_x, \qquad (1)$$

where the subscripts denote partial derivatives with respect to space $x$ and time $t$. The dependent variable $U(x,t) \in \mathbb{R}$ is defined on $x \in [-L/2, L/2]$, where $L$ represents the length of the Taylor column. The parameter $\mu$ represents the forcing $R - R_c$. The particular form of the linear part of this equation ensures (in the absence of boundary effects) the onset of a pattern with wave number 1 at $\mu = 0$. The usual form of the Swift–Hohenberg equation has only a cubic nonlinearity, but we include a quadratic term to ensure there is no $U \to -U$ symmetry (see, e.g., [2, eq. (7.21)]. This term also makes the model equation non-variational and so allows unsteady behaviour as an asymptotic state (though we focus entirely on steady states).

In order to relate the order parameter $U$ to the fluid flow, we interpret $U$ as a stream function, and so $U_x$ represents the radial velocity in the column. The effect of the non-slip boundary conditions on the top and bottom plates is to induce an inwards flow near the boundaries, although the radial velocity is zero on the boundaries themselves. We model this strong forcing at the end walls with the inhomogeneous boundary conditions

$$U(-L/2) = U(L/2) = 0, \qquad U_x(-L/2) = U_x(L/2) = -1. \qquad (2)$$

Similar inhomogeneous boundary conditions were used for example in [21,22]. The only symmetry that remains in the problem is then reflection in the equatorial mid-plane of the apparatus

$$(U, x) \to (-U, -x). \qquad (3)$$

We also consider idealised reflecting boundary conditions

$$U(-L/2) = U(L/2) = 0, \qquad U_{xx}(-L/2) = U_{xx}(L/2) = 0, \qquad (4)$$

which have an additional hidden symmetry [25]. That is, the problem can be extended by reflection onto the domain $x \in [-L, L]$ with periodic boundary conditions and so acquires a continuous translation symmetry. It is this translation symmetry that is broken in the pitchfork bifurcation in the idealised version of this problem with boundary conditions (4) (see figure 1(a)). However, with the inhomogeneous boundary conditions (2), this translation symmetry is broken *a priori* for all solution states.

Experiments find states where the mid-plane reflection symmetry is preserved, so we focus on this case by using reflecting boundary conditions at $x = 0$. We are also interested in examining the transition from idealised to realistic

6

boundary conditions, and so we use

$$U(0) = U_{xx}(0) = U(L/2) = \tau\left(U_x(L/2) + 1\right) + (1 - \tau)U_{xx}(L/2) = 0. \quad (5)$$

Here $\tau$ ($0 \leq \tau \leq 1$) is a Schaeffer homotopy parameter, such that $\tau = 0$ corresponds to the ideal problem (with hidden translation symmetry) and $\tau = 1$ to the realistic non-slip boundary conditions.

## 3   Linear analysis: pitchfork and Hamiltonian Hopf

Consider equation (1) without nonlinear terms. Solutions can be written in terms of exponentials in time and space, of the form

$$U(x,t) = e^{st + (\sigma + ik)x}, \quad (6)$$

where $s$ is the temporal growth rate, $k$ is a spatial wavenumber, and $\sigma$ is a spatial growth rate. In general, $s$ could be complex, but we consider only real $s$, focusing exclusively on steady states. In order to satisfy the linearisation of (1), $s$, $\sigma$ and $k$ must satisfy

$$0 = k\sigma(k^2 - \sigma^2 - 1), \qquad s = \mu - (k^2 - \sigma^2 - 1)^2 + 4\sigma^2 k^2, \quad (7)$$

which can be rearranged to give three possibilities:

$$\text{I}: \qquad k = 0, \qquad s = \mu - (1 + \sigma^2)^2, \quad (8)$$
$$\text{II}: \qquad \sigma = 0, \qquad s = \mu - (1 - k^2)^2, \quad (9)$$
$$\text{III}: \quad k^2 = \sigma^2 + 1, \qquad s = \mu + 4\sigma^2(1 + \sigma^2). \quad (10)$$

Since the linearisation of the PDE (1) is of first order in time and fourth order in space, there is a unique temporal growth rate $s$ and a total of four complex spatial growth rates, which are roots of the equations above. Specifically, in case I these roots are of the form $\pm\sigma_1$ and $\pm\sigma_2$; in case II they take the form $\pm ik_1$ and $\pm ik_2$; and in case III $\pm\sigma \pm ik$. Corresponding to these, the linear solutions are of the form

$$\text{I}: \qquad U(x,t) = e^{st}\left(A\sinh(\sigma_1 x) + B\sinh(\sigma_2 x)\right), \quad (11)$$
$$\text{II}: \qquad U(x,t) = e^{st}\left(A\sin(k_1 x) + B\sin(k_2 x)\right), \quad (12)$$
$$\text{III}: \quad U(x,t) = e^{st}\left(A\cos(kx)\sinh(\sigma x) + B\sin(kx)\cosh(\sigma x)\right), \quad (13)$$

where $A$ and $B$ are constants that will be determined by the boundary conditions at $x = L/2$. The odd boundary conditions at $x = 0$ have already been enforced by the choice of trigonometric functions.
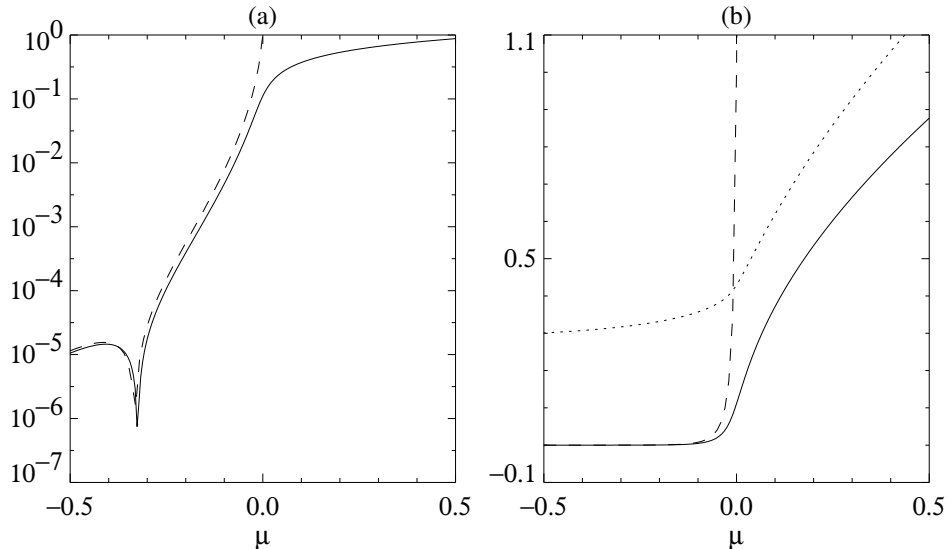
Fig. 3. Dependence of the radial velocity at the midpoint ($U_x(0)$) on the bifurcation parameter $\mu$ for the nonlinear (solid) and linearised (dashed) PDE (1), with $L = 22\pi$ and realistic boundary conditions ($\tau = 1$). Panel (a) shows solutions on a log scale, and (b) on a linear scale. Also shown in (b) as a dotted line is an integrated average of the nonlinear solution and its first three derivatives.

The next stage of the calculation depends on whether ideal ($\tau = 0$) or realistic ($\tau = 1$) boundary conditions are being used. With ideal boundary conditions, $U = 0$ is always a solution of (1), and bifurcations from this state occur when there are marginally stable ($s = 0$) linear solutions. Setting $s = 0$ and $U(L/2) = U_{xx}(L/2) = 0$ results in no solution in cases I and III, and an eigenvalue problem in case II, where $k$ can take on discrete values: $k = 2\pi n/L$, where $n$ is the number of vortices in the half-domain. There are thus pitchfork bifurcations at

$$\mu_{\mathrm{pf}} = \left(1 - \left(\frac{2\pi n}{L}\right)^2\right)^2, \tag{14}$$

for any integer $n$. In particular, there is a pitchfork bifurcation at $\mu = 0$ whenever the domain is chosen to fit an exact number of vortices: $n = L/2\pi$. Note that the condition for the onset of the vortices is $s = 0$ and $\sigma = 0$, with a purely imaginary spatial wavenumber $\pm ik$ corresponding to a spatially periodic pattern. On either side of this bifurcation point, the temporal growth rate $s$, indicating the stability of the Couette flow, changes from negative to positive at the pitchfork bifurcation.

On the other hand, with inhomogeneous boundary conditions ($\tau = 1$), there are nonzero steady ($s = 0$) linear solutions for all values of $\mu$. Case I can only arise when $\mu \geq 1$ (and in fact only a single solution is possible); in case II, there are two possible solutions for $0 \leq \mu \leq 1$ and one for $\mu > 1$, and case III is possible only when $\mu \leq 0$. The solutions are thus, for $\mu < 0$: $U(x) = A\cos(kx)\sinh(\sigma x) + B\sin(kx)\cosh(\sigma x)$, where $\sigma > 0$ and $k > 0$ are determined from $\mu$ by $4\sigma^4 + 4\sigma^2 + \mu = 0$ and $k^2 = 1 + \sigma^2$; and for $0 < \mu < 1$:

8

$U(x) = A \sin(k_1 x) + B \sin(k_2 x)$, where $k_1 > 0$, $k_2 > 0$ and $k_1^2 = 1 + \sqrt{\mu}$, $k_2^2 = 1 - \sqrt{\mu}$. In these two expressions for $U(x)$, the constants $A$ and $B$ are determined by a pair of linear equations from the boundary conditions $U(L/2) = 0$ and $U_x(L/2) = -1$.

For illustration purposes let us focus on the case $L = 22\pi$. The dependence on $\mu$ of the solution, as measured by the radial velocity at the midpoint ($U_x(0) = A\sigma + Bk$ for $\mu < 0$, and $U_x(0) = Ak_1 + Bk_2$ for $0 < \mu < 1$) is shown as a dashed line in figure 3. The amplitude of the linear solution goes to infinity for $\mu$ about 0.00826.

Since there is no sharp onset with realistic boundaries, one cannot define a precise value of $\mu$ at which pattern will be first observed in a domain of finite length, but the value of $\mu = \mu_\infty$ for which the linear solution goes to infinity is a suitable proxy. This is defined implicitly by the condition

$$(k_1 + k_2) \sin\left((k_1 - k_2)\frac{L}{2}\right) = (k_1 - k_2) \sin\left((k_1 + k_2)\frac{L}{2}\right), \qquad (15)$$

where $k_{1,2}$ are defined in terms of $\mu$ above. When $L$ is large, the smallest positive solution $\mu_\infty$ occurs when $(k_1 - k_2)L/2 = \pi$. This yields

$$\mu_\infty = \frac{4\pi^2}{L^2} + O(L^{-3}). \qquad (16)$$

In other words, the divergence of the linear solution occurs for $\mu$ closer to zero as $L$ increases. Moreover, we have that for large $L$ the first pitchfork bifurcation occurs at

$$\mu_{\mathrm{pf}} = \frac{4\delta^2}{L^2} + O(L^{-3}), \quad \text{where} \quad \delta = L - 2\pi\left[L/(2\pi)\right], \qquad (17)$$

so $|\delta| < 2\pi$. Hence $\mu_\infty$, $\mu_{\mathrm{pf}}$ and the difference between them are all of the same order: $L^{-2}$.

Also shown in figure 3 are nonlinear solutions of (1). The linear and nonlinear solutions are close to each other for $\mu$ negative: the slight discrepancy arises because the linearised solution is not small close to the boundaries. However we do note that the point at which the amplitude of the nonlinear solution (as measured by the radial velocity at the midpoint) becomes significant is well predicted by the blow-up point of the linear solution. Note also from the figure (specifically the dotted line in figure 3(b)), that other measures of amplitude that take into account the global amplitude of the solution (not only at the midpoint) show the rise in amplitude to be much more gradual.

Linear solutions of the PDE (1) are shown in figure 4 for two values of $\mu$. As $\mu$ is increased from negative values to $\mu = 0$, the exponentially decaying linear
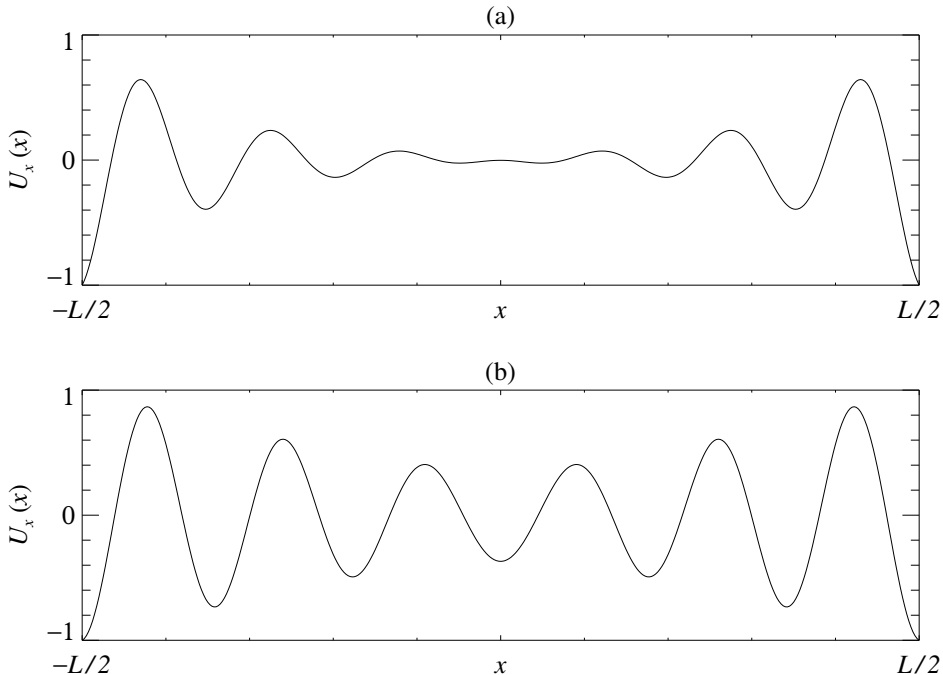
Fig. 4. Linear solutions of (1), with $L = 40$ and $\tau = 1$, with (a) $\mu = -0.1$ and (b) $\mu = 0$, showing the growth of the solution in from the edges ($x = \pm L/2$). Compare with figure 2.

solution extends further into the bulk of the fluid. In an arbitrarily long cylinder, the radial velocity at the midpoint of the apparatus would remain almost zero until the spatial decay rate (as measured by $\sigma$) became zero. Therefore, the condition for onset of steady vortices, as measured at the midpoint of the apparatus, is $\sigma = 0$ and $s = 0$ – which is the same condition as for the onset of vortices with the idealised boundary conditions. In this case, however, on either side of onset, it is the spatial eigenvalues $\pm\sigma \pm ik$ and $\pm ik_1$, $\pm ik_2$ that change in nature, at a Hamiltonian Hopf bifurcation [26] (see figure 5).

More accurately, we should describe the spatial bifurcation as a reversible 1:1 resonance, since the ODE obtained by setting $U_t = 0$ in (1) does not conserve a first integral and so cannot correspond to a Hamiltonian system. Nevertheless, the reflection symmetry (3) implies that the steady problem is reversible in the sense analysed by Iooss and Peroueme [27]. They show that the unfolding of such a normal form is essentially identical to that of the Hamiltonian case (although there are differences in the beyond-all-orders terms). In their notation, the spatial bifurcation we have here is supercritical. Hence for $\mu > 0$ there exist spatially periodic solutions the maximum amplitude of which grows as the square root of $\mu$ for the nonlinear problem. The implications of this bifurcation are discussed in more detail in Section 5.

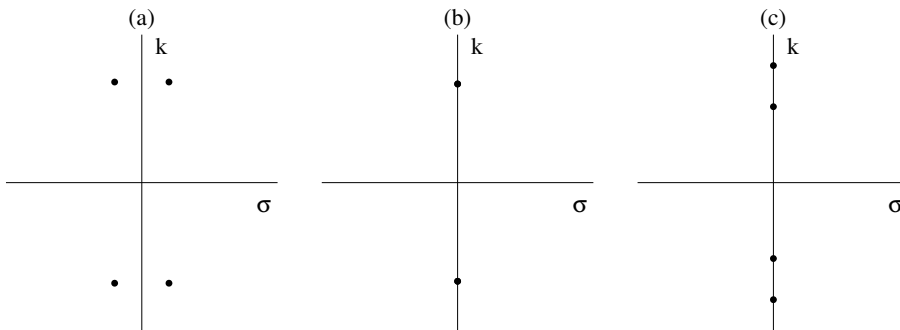This explanation carries over from the Swift–Hohenberg model to the Taylor–

Fig. 5. Hamiltonian Hopf bifurcation: (a) $\mu < 0$, the spatial eigenvalues are $\pm\sigma \pm ik$; (b) $\mu = 0$, the eigenvalues $\pm i$; (c) $\mu > 0$, the eigenvalues are $\pm ik_1$, $\pm ik_2$.

Couette problem and more general pattern forming situations with strong forcing at the boundaries. If one assumes periodic boundary conditions, with pure imaginary spatial wavenumbers, the criterion for onset in a general pattern forming problem is that the temporal growth rate is zero. If, on the other hand, one takes the end walls into account but the domain is very large, and the pattern is measured only far away from the boundaries, then the steady inhomogeneous solution will penetrate into the bulk of the fluid and reach the centre when the real part of the spatial wavenumber is zero. Thus the two perspectives will yield the same condition for the onset of pattern formation: $\mu = 0$ in the case of the model PDE, or $R = R_c$ in the case of Taylor–Couette flow. This explains the sharp transition seen in large domain Taylor–Couette experiments at the Reynolds number predicted using idealised boundary conditions, even though the boundaries are forcing the flow strongly.

## 4   Nonlinear steady-state bifurcation analysis

The remaining issues to be addressed are the effect of the length of the domain on the nonlinear solutions, and the location of the saddle-node bifurcation on the anomalous branch (figure 1(c)).

We focus on the steady state problem given by setting $U_t = 0$ in (1).

$$U_{xxxx} + 2U_{xx} + (1 - \mu)U + U^3 + U\,U_x = 0, \tag{18}$$

subject to boundary conditions (5). Nonlinear solutions are computed using AUTO [28] as a boundary value solver. The effect of the size of the domain is illustrated in figures 6 and 7. As the length $L$ increases, the amplitude, as measured in the centre, sets in more sharply as $\mu$ is increased through zero, and the curve resembles half a pitchfork as $L \to \infty$. With very large values of $L$ (figure 7), the exponential decay into the bulk ensures that the
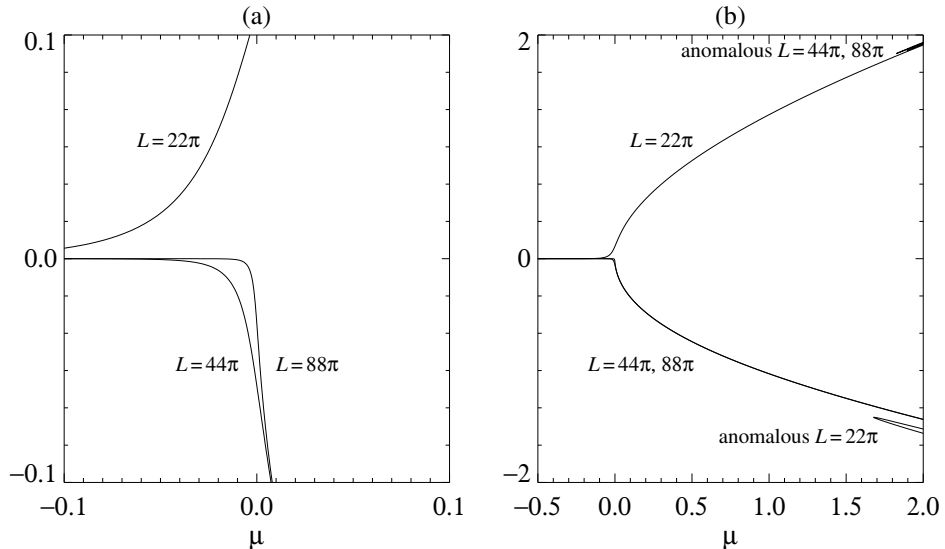
11

Fig. 6. As the length of the domain increases, the pattern, as measured in the centre, sets in more sharply: (a) detail near $\mu = 0$, for $L = 22\pi$, $44\pi$ and $88\pi$; (b) the larger picture, showing the anomalous modes.

inhomogeneous pattern has very small amplitude for $\mu \leq 0$. This is consistent with our understanding from the linear theory. The anomalous mode branches for $L = 22\pi$, $44\pi$ and $88\pi$ are also shown in figure 6. Note how the anomalous modes do not approach $\mu = 0$ for larger values of $L$, even though the symmetry-breaking effects are being pushed further away.

With a fixed value of $L$, only one sign of $U_x(0)$ is possible near the transition at $\mu = 0$, but which one is observed depends whether the number of vortices between $x = 0$ and $x = L/2$ is even or odd.

Next, we consider the connection between pitchfork bifurcations (in the case of ideal boundary conditions) and saddle-node bifurcations (in the case of realistic boundary conditions). With ideal boundary conditions, pitchforks occur both from the trivial solution and as secondary bifurcations from the various primary branches. We concentrate on the case $L = 22\pi$. Figure 8 shows the bifurcation diagram computed with ideal (a,b: $\tau = 0$) and realistic (c: $\tau = 1$) boundary conditions. Bifurcation points from the trivial solution (and secondary bifurcations from the primary branches) are marked in the figure. The primary bifurcation points occur at $\mu = \mu_{\mathrm{pf}}$ (14), with the bifurcating branch being locally proportional to $\sqrt{\mu - \mu_{\mathrm{pf}}} \sin(n\pi/L)$. With $L = 22\pi$, the solution with $n = 11$ bifurcates precisely from $\mu = 0$ and corresponds to a pattern with 11 vortices in the half domain. The next four bifurcating branches for positive $\mu$ are also shown in the figure. These bifurcate at $\mu = 0.0301$, $0.0361$, $0.1093$ and $0.1574$ and correspond to $n = 10$, $12$, $9$, and $13$ vortices respectively. Note that these solutions are invariant under reflections in the midpoint ($x = 0$), and are spatially periodic with period $2L/n$.
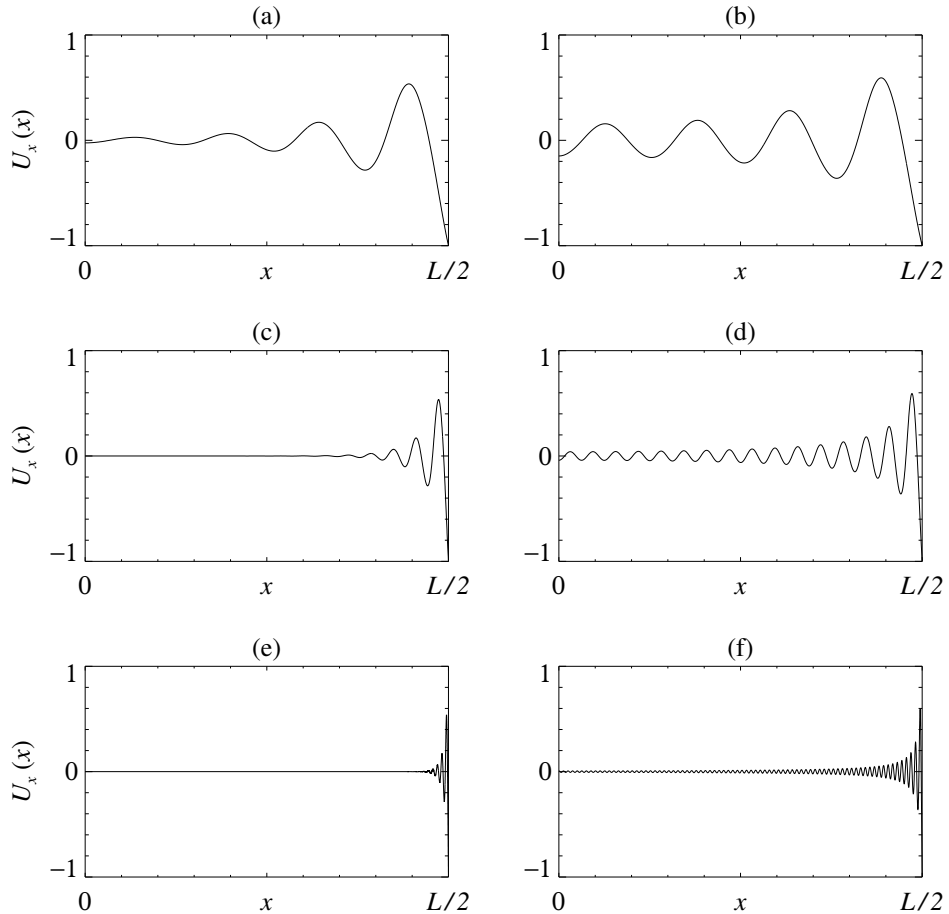
12

Fig. 7. As $\mu$ increases through zero, the wall mode penetrates further into the bulk, but the amplitude at the centre of the domain remains small for larger values of $L$. (a,b) $L = 50$, $\mu = -0.1$, 0; (c,d) $L = 200$, $\mu = -0.1$, 0; (e,f) $L = 1000$, $\mu = -0.1$, 0. These are nonlinear solutions, but linear solutions for $\mu = -0.1$ look very similar.

Figure 8(c) shows a few of the many branches that exist for realistic boundary conditions ($\tau = 1$), in the same parameter range as figure 8(b). These were obtained by taking all the points on the branches in figure 8(b) with $\mu = 2$ and continuing these to $\tau = 1$, and then continuing in $\mu$ once more. Note that all of the pitchfork bifurcations have been destroyed, and have been replaced by a series of saddle-node bifurcations. The fundamental pitchfork bifurcation at $\mu = 0$ has been replaced by a smooth transition, though the remnant of the pitchfork shape can clearly be seen, and there is a sharp rise in amplitude close to $\mu = 0$ as predicted by the linear theory of the preceding section. Nonlinear solution profiles on this fundamental branch (figure 9(b)) are qualitatively similar to those with ideal boundary condition (figure 9(a)), and so might be said to correspond to $n = 11$ vortices. Figure 9(c) shows normal and anomalous modes at the same parameter value, illustrating how the difference between the two concentrated near the boundary translates into a phase shift in the bulk.
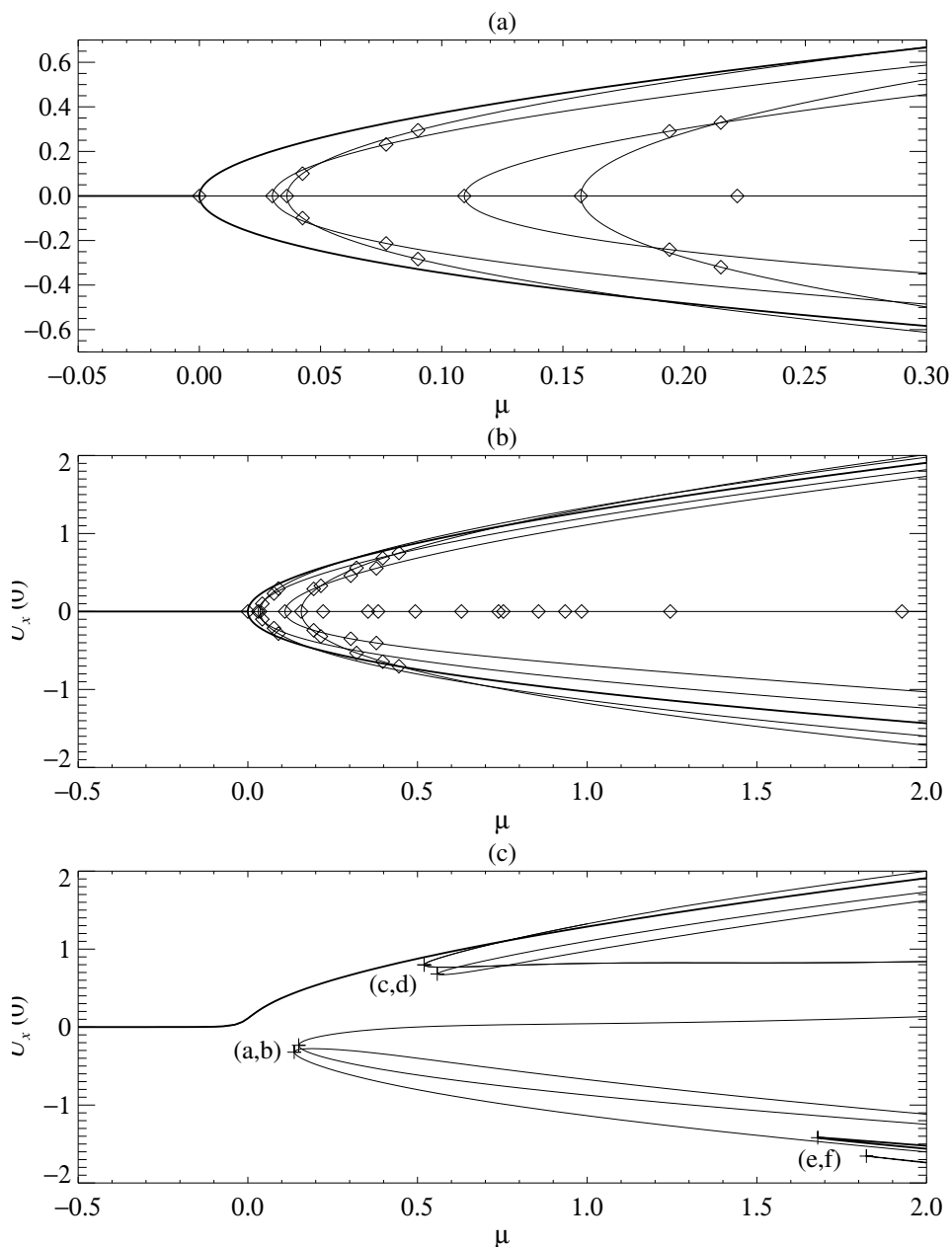
13

Fig. 8. (a,b) The idealised bifurcation diagram with $\tau = 0$ and $L = 22\pi$: $U_x(0)$ as a function of bifurcation parameter $\mu$. Diamonds represent pitchfork bifurcation points. Only the first five bifurcating branches from the trivial solution are depicted. In increasing order of $\mu$, these have 11, 10, 12, 9 and 13 pairs of vortices in the full domain. (c) Bifurcation diagram with $\tau = 1$, showing the smooth onset of the 11 vortex solution, and several disconnected branches. The plus signs indicate solutions that are depicted in figure 10(a–f), at saddle-node bifurcation points. The thick lines represent branches that are known to be stable.
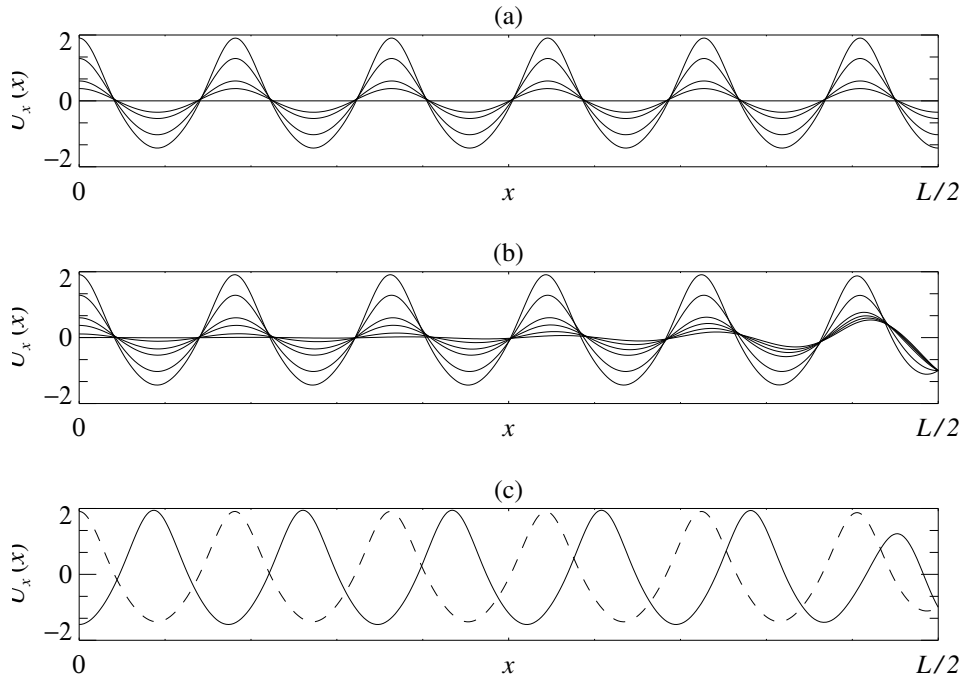
14

Fig. 9. Examples of $n = 11$ vortex solutions with (a) ideal ($\tau = 0$) and (b) realistic ($\tau = 1$) boundary conditions, with $\mu = 2$ (largest amplitude), $\mu = 1$, $\mu = 0.25$, $\mu = 0.1$, $\mu = 0$, $\mu = -0.1$. (c) Example of normal (dashed) and anomalous (solid) modes with $\mu = 2$ and realistic boundary conditions.

This now brings us to the question of the supposed disconnected part of the unfolded pitchfork. Examples of solutions at the labelled saddle-node bifurcation points are shown in figure 10(a–h), with the solution $U_x(x)$ at the saddle-node bifurcation points drawn as solid lines. These saddle-node bifurcations were then continued in $(\mu, \tau)$ back to $\tau = 0$ to discover from where they originate. Most connect to secondary bifurcations in figure 8(a) and therefore represent unstable solutions (and are shown as dashed lines in figure 10). However, the saddle-node bifurcation on the stable anomalous 11 vortex branch, shown in figure 10(e) is found to create a stable branch. (The stability of a typical solution on this branch was checked by solving, in addition to the ODEs (18), the linear variational equations governing a temporal eigenmode with eigenvalue $s$. AUTO was then used to continue solutions in $s$ to establish that there are no nontrivial solutions for $s > 0$.) Unexpected behaviour was found for this branch upon varying the homotopy parameter $\tau$. One might imagine that under homotopy to $\tau = 0$ this saddle-node bifurcation point should approach the fundamental pitchfork bifurcation at $\mu = 0$. This is not the case for these parameter values. When $\tau$ is reduced from 1 to 0, the saddle-node bifurcation itself undergoes a pair of folds with respect to $\mu$ (see figure 11), and ends up (at $\tau = 0$) in the unfolding of the $n = 12$ bifurcation point at $\mu = 0.0425$ (the dashed profile in figure 10(e) corresponds to a 12 vortex pattern).
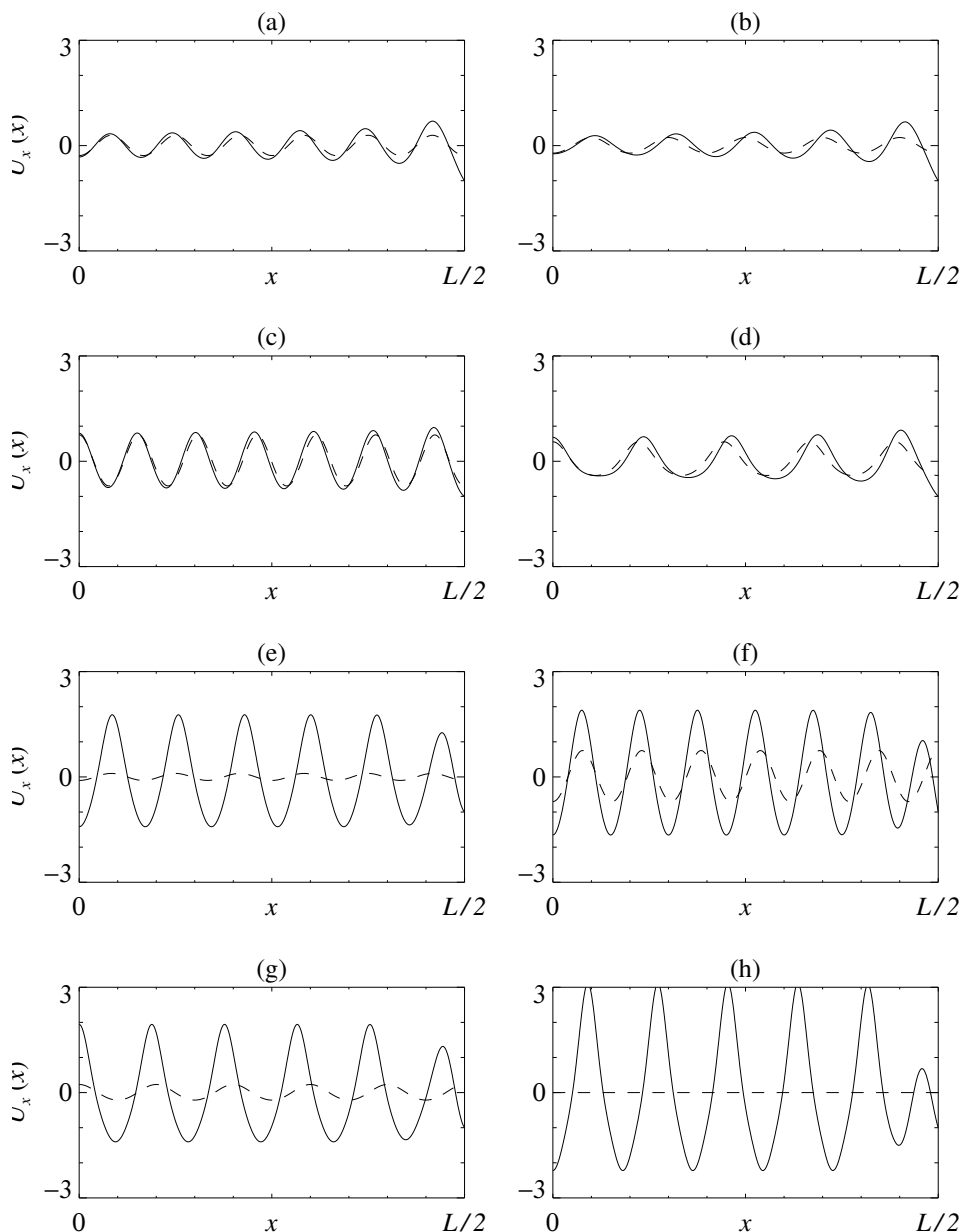
15

Fig. 10. Examples of solutions at the labelled saddle-node bifurcation points from figure 8(c). (g,h) are outside the range shown in figure 8. Solid lines depict the solution at the saddle node bifurcation with $\tau = 1$, and dashed lines show the solution that has been continued to $\tau \to 0$, ending up at one of the bifurcation points in figure 8(a). (a) $\mu = 0.1367 \to 0.0901$; (b) $\mu = 0.1498 \to 0.0770$; (c) $\mu = 0.5193 \to 0.4452$; (d) $\mu = 0.5581 \to 0.3787$; (e) $\mu = 1.6794 \to 0.0425$; (f) $\mu = 1.8227 \to 0.4452$; (g) $\mu = 2.1318 \to 0.0770$; (h) $\mu = 4.6220 \to 0.0000$. The last case is illustrated in more detail in figure 12. The saddle-node in (e) involves the creation of the stable 11-vortex anomalous branch.
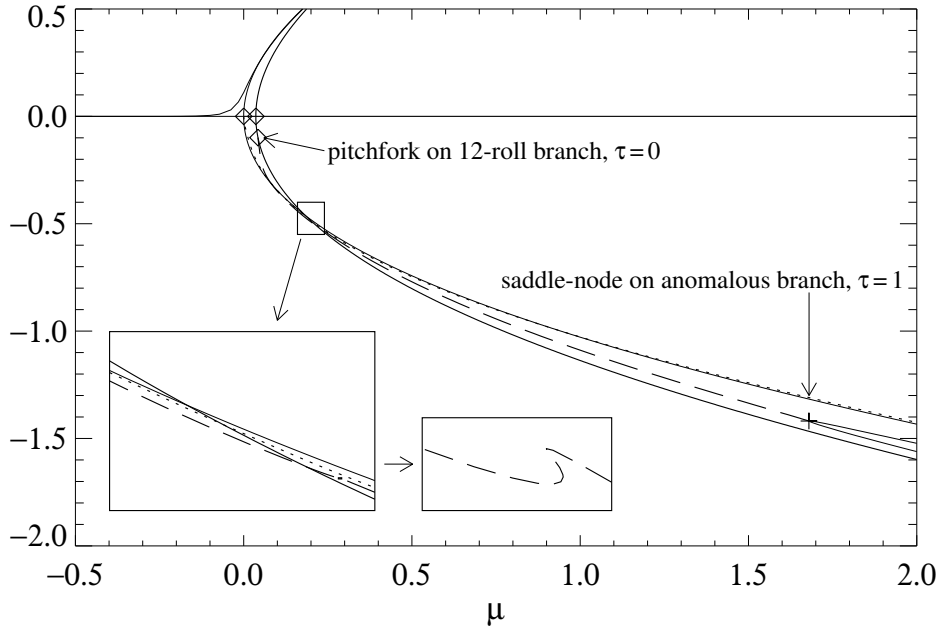
Fig. 11. Path of the saddle-node bifurcation (dashed line) starting at $\tau = 1$ in the saddle-node bifurcation on the stable anomalous branch, and ending at $\tau = 0$ at a pitchfork bifurcation point on the 12 vortex branch. At either end, the solutions are depicted in figure 10(e). The two insets show successive enlargements, and reveal a pair of folds on route. The solid lines are the 11 and 12 vortex branches ($\tau = 0$), and the dotted line is the route of the saddle-node bifurcation that starts at the primary bifurcation point $\mu = 0$ at $\tau = 0$.

Alternatively, one could try following the saddle-node bifurcation point that occurs as one unfolds the pitchfork at $\mu = 0$ under infinitesimal increase of $\tau$ from zero. When this is done, the saddle-node bifurcation can be continued up to $(\mu, \tau) = (4.6220, 1)$ – see the dotted line in figure 11, and examples of solutions in figure 10(h) and figure 12.

The details of which saddle-node bifurcation (with $\tau = 1$) connects to which pitchfork bifurcation (with $\tau = 0$) was found to depend sensitively on the value of $L$. For example, with $L = 88\pi$, the saddle-node bifurcation on the 44 vortex anomalous branch does continue down to the primary pitchfork to 44 vortices at $\mu = 0$, though in this case the anomalous branch is not stable. The details of how the branches connect also depends on the particular choice how the ideal and realistic boundary conditions are combined via homotopy. For example replacing the ultimate '+' in (5) with a '−' leads to significantly different results.
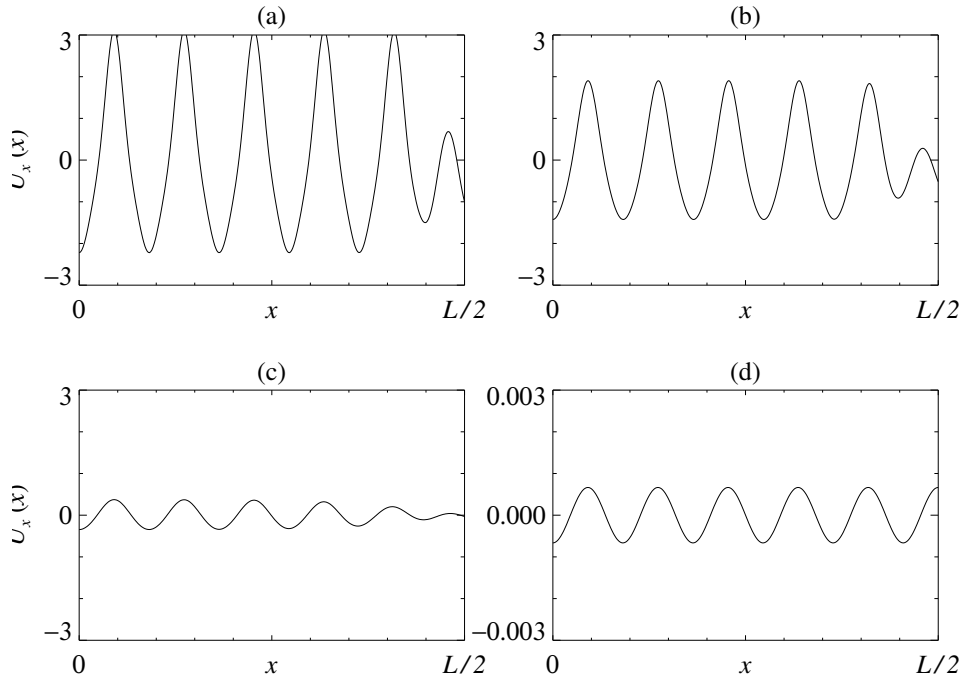
17

Fig. 12. Continuation of the saddle-node bifurcation: (a) $(\mu, \tau) = (4.622, 1.000)$, (b) $(\mu, \tau) = (2.000, 0.597)$, (c) $(\mu, \tau) = (0.100, 0.076)$, (d) $(\mu, \tau) \approx (0.000, 0.000)$.

## 5 Conclusion

The apparent contradiction described in the introduction is resolved, at least in the context of the Swift–Hohenberg model considered here. The onset of Taylor vortices is not a weakly broken pitchfork bifurcation, because of the strong symmetry-breaking induced by the inhomogeneous boundary forcing. Anomalous modes stay bounded away from the critical value of the bifurcation parameter as they must overcome the strong preference set by the boundary. When the amplitude of the pattern is measured far away from the boundaries, the pattern appears to set in sharply, in half a pitchfork bifurcation, as the decaying wall mode penetrates the bulk of the domain. The parameter value at which pattern, as measured in the centre of a large domain, becomes of significant amplitude is the same as the value predicted assuming idealised boundary conditions, because the requirements for both situations are the same: steady ($s = 0$) and zero spatial growth rate ($\sigma = 0$). Moreover we have shown that for a long but finite domain of length $L$, that the parameter value corresponding to this large central growth in pattern occurs according to linear theory at a value that is within $O(L^{-2})$ of the idealised pitchfork.

The ideas were developed for the model equation, but they apply equally well to the Taylor–Couette case, and resolve the difficulties raised by Benjamin and Mullin [8]. It should be noted that the Swift–Hohenberg equation

we have analysed is intended only to be a *qualitative* model of the Taylor–Couette experiment: it is the simplest pattern-forming PDE that is appropriate for steady patterns forming with a non-zero wavelength. In contrast, the Ginzburg–Landau equation for the complex amplitude $A(X, T)$,

$$A_T = \mu A + A_{XX} - |A|^2 A, \tag{19}$$

describes the *envelope* of the pattern: $U(x, t) = \Re(A(X, T)e^{ix})$, where $X$ and $T$ are a long length scale and a slow time scale. The Ginzburg–Landau equation does not distinguish between normal and anomalous modes, since anomalous modes involve a change near the boundaries on the length scale of the pattern, rather than the length scale of the modulation (as in figure 9(c)). However, with an $O(1)$ inhomogeneous boundary condition, the Ginzburg–Landau equation provides a *quantitative* description of the smooth onset of Taylor vortices [21]. The Swift–Hohenberg model may also provide a quantitative description of onset (perhaps with different choices of nonlinear terms and boundary conditions), but we do not expect quantitative agreement with large amplitude anomalous modes.

We have also observed that the saddle-node bifurcation on the anomalous branch does not necessarily connect to the primary bifurcation as boundary conditions vary from real to ideal. The specific results described here apply only to the Swift–Hohenberg model, though the general conclusion that we can make is that, under small perturbations from the ideal boundary conditions, we expect the pitchfork to be perturbed in the generic way, as in figure 1(b). However, going all the way to $\tau = 1$ is not a small perturbation, and in general nothing can be said about whether the the saddle-node bifurcation created in the unfolding of the primary pitchfork is the same (or not the same) as the saddle-node at the end of the stable anomalous branch, or even if there is an anomalous branch that is stable.

This approach yields results that are applicable to other pattern formation problems (for instance, Rayleigh–Bénard convection). Earlier work on convection [18,19] has focused on weak forcing at the side walls, primarily using Swift–Hohenberg theory. We have shown here how the ideas can be extended to strong forcing.

An interesting aspect of our work has been to link the mode selection problem to the existence of a spatial Hamiltonian Hopf bifurcation for the infinite length problem. Note that four spatial derivatives are necessary for a spatial Hamiltonian Hopf bifurcation, and indeed four spatial derivatives are necessary for pattern formation at a non-zero wave number, if the marginal stability curve is to have a minimum at non-zero wave number. The Hamiltonian Hopf bifurcation gives the possibility of the existence of branches of spatially periodic solutions beyond the critical parameter value for the onset of rolls, whose period for small amplitude is that given by the wave number of the neutral

mode of the temporal problem. The normal form of the Hamiltonian Hopf bifurcation (even for reversible systems) is completely integrable up to any order (see e.g., [27]) and instead of a unique spatially periodic solution, there is a one parameter band of spatially periodic solutions, whose envelope grows as the square root of the bifurcation parameter $\mu$. There also exists a two-parameter family of spatially quasi-periodic solutions whose existence is bounded by the periodic solutions and homoclinic connections to them. However, in the reversible case, not all these solutions will necessarily exist in a full unfolding of the normal form that breaks its Hamiltonian structure. We note, from our numerical results for the nonlinear problem with realistic boundary conditions and fixed $L$, that the main branch seems to develop a connection from the boundary to a pure periodic state in the middle of the domain. It is not clear *a priori* why this solution and not others are selected from the unfolding of the Hamiltonian Hopf bifurcation.

Finally, we mention another outstanding issue in the problem of the onset of Taylor vortices [11]: the timescales for the onset and decay of the pattern are different. In particular, the authors of [11] computed steady solutions at Reynolds numbers just above and just below critical, and in each case altered the Reynolds number to an intermediate value and examined the transient. In the case of onset, the pattern invaded the bulk as a front travelling in from the boundary, while in the case of decay, there was uniform decay throughout bulk. The timescales for these two processes were different, inconsistent with an explanation in terms of a Ginzberg–Landau equation. It may be possible to explain this using a Swift–Hohenberg based model such as considered here. This issue will be taken up in future work.

## Acknowledgements

## References

[1] R.C. Di Prima, H.L. Swinney, Instabilities and transition in flow between concentric rotating cylinders, in: H.L. Swinney, J.P. Gollub (Eds.), Hydrodynamic Instabilities and the Transition to Turbulence, Springer, Berlin, 1981, pp. 139–180.

[2] E.L. Koschmieder, Bénard Cells and Taylor Vortices, CUP, Cambridge, 1993.

[3] P. Chossat, G. Iooss, The Couette–Taylor Problem, Springer, New York, 1994.

[4] R. Tagg, The Couette–Taylor problem, Nonlinear Science Today 4 (1994) 1–25.

[5] G.I. Taylor, Stability of a viscous liquid contained between two rotating cylinders, Phil. Trans. R. Soc. Lond. A 223 (1923) 289–343.

[6] J.P. Gollub, M.H. Freilich, Optical heterodyne test of perturbation expansions for the Taylor instability, Phys. Fluids 19 (1976) 618–626.

[7] T.B. Benjamin, Bifurcation phenomena in steady flows of a viscous liquid. I. Theory, Proc. R. Soc. Lond. A 359 (1978) 1–26.

[8] T.B. Benjamin, T. Mullin, Anomalous modes in the Taylor experiment, Proc. R. Soc. Lond. A 377 (1981) 221–249.

[9] D. Coles, Transition in circular Couette flow, J. Fluid Mech. 21 (1965) 385–425.

[10] T. Alizary de Roquefort, G. Grillaud, Computation of Taylor vortex flow by a transient implicit method, Computers and Fluids 6 (1978) 259–269.

[11] J. Abshagen, O. Meincke, G. Pfister, K.A. Cliffe, T. Mullin, Transient dynamics at the onset of Taylor vortices, J. Fluid Mech. 476 (2003) 335–343.

[12] D. Schaeffer, Qualitative analysis of a model for boundary effects in the Taylor problem, Math. Proc. Camb. Phil. Soc. 87 (1980) 307–337.

[13] T.B. Benjamin, Bifurcation phenomena in steady flows of a viscous liquid. II. Experiment, Proc. R. Soc. Lond. A 359 (1978) 27–43.

[14] J.H. Bolstad, H.B. Keller, Computation of anomalous modes in the Taylor experiment, J. Comput. Phys. 69 (1987) 230–251.

[15] K.A. Cliffe, T. Mullin, A numerical and experimental study of anomalous modes in the Taylor experiment, J. Fluid Mech. 153 (1985) 243–258.

[16] K.A. Cliffe, J.J. Kobine, T. Mullin, The role of anomalous modes in Taylor–Couette flow, Proc. R. Soc. Lond. A 439 (1992) 341–357.

[17] A. Lorenzen, T. Mullin, Anomalous modes and finite-length effects in Taylor–Couette flow, Phys. Rev. A 31 (1985) 3463–3465.

[18] P.G. Daniels, The effect of distant sidewalls on the transition to finite amplitude B■nard convection, Proc. R. Soc. Lond. A 358 (1977) 173–197.

[19] P.G. Daniels, D. Ho, A.C. Skeldon, Solutions for nonlinear convection in the presence of a lateral boundary, Physica D 178 (2003) 83–102.

[20] G. Pfister, I. Rehberg, Space-dependent order parameter in circular Couette flow transitions, Phys. Lett. A 83 (1981) 19–22.

[21] G. Ahlers, D.S. Cannell, M.A. Dominguez-Lerma, R. Heinrichs, Wavenumber selection and Eckhaus instability in Couette–Taylor flow, Physica D 23 (1986) 202–219.

[22] R. Graham, J.A. Domaradzki, Local amplitude equation of Taylor vortices and its boundary condition, Phys. Rev. A 26 (1982) 1572–1579.

[23] J. Swift, P.C. Hohenberg, Hydrodynamic fluctuations at the convective instability, Phys. Rev. A 15 (1977) 319–328.

[24] I. Melbourne, Steady-state bifurcation with Euclidean symmetry, Trans. Am. Math. Soc. 351 (1999) 1575–1603.

[25] M. Golubitsky, J. Marsden, D. Schaeffer, Bifurcation problems with hidden symmetries, in: W.E. Fitzgibbon III (Ed.), Partial Differential Equations and Dynamical Systems, Pitman, Boston, 1984, pp. 181–210.

[26] J. van der Meer, The Hamiltonian Hopf bifurcation, Lecture Notes in Mathematics 1160, Springer-Verlag, Berlin, 1985.

[27] G. Iooss, M.C. Peroueme, Perturbed homoclinic solutions in reversible 1:1 resonance vector fields, J. Diff. Eq. 102 (1993) 62–88.

[28] E.J Doedel, A.R. Champneys, T.R. Fairgrieve, Yu.A. Kuznetsov, B. Sandstede, X.J. Wang, AUTO97 Continuation and bifurcation software for ordinary differential equations (1997).